Cellular (de)coordination in gliding motility and plectoneme formation

Jerko Rosko[1,*], Kelsey Cremin[1,*], Emanuele Locatelli[2,*], Mary Coates[1], Sarah J. N. Duxbury[1], Kieran Randall[1], Katie Croft[1,+], Chantal Valeriani[3], Marco Polin[1,4], and Orkun S. Soyer[1,†]

[1]School of Life Sciences, University of Warwick
[2]Department of Physics and Astronomy, University of Padova, Via Marzolo 8, I-35131 Padova, Italy and INFN, Sezione di Padova, Via Marzolo 8, I-35131 Padova, Italy
[3]Departamento de Estructura de la Materia, Física Termica y Electronica, Facultad de Ciencias Físicas, Universidad Complutense de Madrid, 28040 Madrid, Spain
[4]Instituto Mediterráneo de Estudios Avanzados, IMEDEA, 07190 Esporles, Illes Balears, Spain
[*]These authors contributed equally
[†]Corresponding author, *O.Soyer@warwick.ac.uk*
[+]Current address: Medical Research Council, Weatherall Institute of Molecular Medicine, University of Oxford

February 6, 2024

1 Significance Statement

Gliding motility is seen in diverse bacteria, but the dynamics of this type of motion and the molecular mechanisms creating propulsive forces are still not fully understood. In some gliding cyanobacteria, many cells remain attached to each other to form a single filament, thus necessitating an intra-cellular coordination of propulsive forces. To better understand such coordination, we study here the dynamics of gliding motility in a filamentous cyanobacteria. We find that, on agar surface, gliding filaments move back-and-forth in a well-defined trajectory and their translation is coupled with rotation along the long axis of the filament. During reversals, cells mostly remain coordinated with each other. These dynamics are captured by a physical model, which predicts that a loss of cell-to-cell coordination can cause loss of smooth reversal. Confirming this prediction, we find that longer filaments can readily get de-coordinated during reversals, resulting in the buckling of filaments and formation of plectonemes. These experimental results and the developed model will inform future studies of molecular mechanisms in single filaments and collective behaviors of many filaments.

2 Abstract

Gliding motility involves a characteristic back-and-forth movement of cells without flagella, and is seen in diverse bacteria. It is currently unknown how reversal dynamics in gliding motility are coordinated, especially in the case of multi-cellular, filamentous cyanobacteria. Here, we study gliding motility dynamics in a recently described species, capable of extensive gliding motility and collective, macro-structure formation. We find that gliding motility involves filaments rotating and translating through slime tubes, rather than on top of slime. On agar, filaments move back-and-forth on well-defined trajectories, where they display a characteristic

speed profile, peaking in the middle of the trajectory. The time spent during each reversal displays a long-tailed distribution, with most reversals being almost instantaneous, while few involve a significant time of no movement. During reversals, individual cells remain mostly coordinated in their motion. Based on these experimental observations, we develop a biophysical model that incorporates cellular propulsive forces, the direction of which is decided by each cell based on mechano-sensing of their neighbors' motion. This model can capture experimental observations and predicts that loss of mechano-sensing can cause de-coordination of filament ends during reversals. In line with this prediction, we find instances of filaments becoming de-coordinated during reversals and that these instances are associated with plectoneme formation. The presented characterisation of filament movement dynamics and the corresponding physical model will inform future studies on individual and collective filament behaviours under different conditions.

3 Introduction

Gliding motility is a specific form of bacterial motility that does not involve flagella [1, 2, 3, 4, 5]. This type of motility is characteristically associated with smooth, back-and-forth movement and is observed in diverse single celled bacteria belonging to the phylum proteobacteria, and in multi-cellular, filamentous cyanobacteria [6]. In several of these organisms, gliding motility is also involved in different collective behaviors, including aggregate formation [7, 8] and collective predation [9].

The absence of flagella in gliding bacteria has led to a research focus in identifying the molecular mechanisms of force generation during gliding. In single celled bacteria, studies in the species *Flavobacterium johnsoniae* and *Myxococcus xanthus* have shown that gliding motility involves membrane-bound protein complexes moving in helical patterns across and around the cell body [10, 11, 12, 13]. As these membrane proteins reach so-called focal adhesion points, at the cell-surface contact, they are suggested to generate axial forces that translate the cell and rotate it around its long axis [14, 4]. Mutational studies in these - and other - species have also identified proteins involved in the biosynthesis and secretion of a sugar polymer, so-called slime, to be essential for gliding motility [1, 2, 3, 4]. In filamentous cyanobacteria, helically organised surface fibril proteins [15, 16, 17, 18] and junctional protein complexes [19] were identified and suggested to link with motility through surface wave formation or slime secretion, respectively [19, 15]. In *Nostoc punctiforme*, where only differentiated filaments called hormogonia display gliding motility, pili proteins are also implicated in motility [20]. Proteins associated with Type IV pili are found to be localised at the cell junctions, leading to the suggestion that the pili action is interlinked with slime excretion [20, 21]. Immunolabelling of pili and staining of slime simultaneously in *N. punctiforme* suggest that the slime trail and pili point to opposite directions, which can be explained by the pulling of pili generating the propulsive force in this species [22]. Recently, a role for pili has been implicated in other filamentous cyanobacteria as well, where deletion of genes relating to Type IV pili machinery is shown to disrupt or abolish motility [23].

Despite these ongoing efforts on the molecular mechanisms of force generation, the dynamics of gliding motility in filamentous cyanobacteria remains poorly characterised. In particular, it is not clear how filamentous cyanobacteria achieve coordination of cellular propulsive forces during gliding and reversals [5]. A better understanding of motility dynamics can provide insights into reversal coordination and inform molecular studies of propulsion. Study of the motility dynamics at the filament level is also relevant to inform population-level observations, such as the recently described aggregate formation [24] and nematic alignment of filaments [25]. Current theroetical explanations for these observations make *ad hoc* assumptions about filament behaviour [24, 25], which can be better justified, or ruled out, upon better understanding of movement and reversal dynamics.

Here, we study gliding and reversal dynamics in a recently described filamentous cyanobacterium *Fluctiforma draycotensis* gen. nov., sp. nov., capable of extensive gliding motility and macro-scale structure formation [26]. In this paper, we focus on characterisation of movement and reversal dynamics, rather than

elucidating their molecular mechanisms. To study movement dynamics, we used extensive time lapse microscopy under phase, fluorescent, and total internal reflection (TIRF) modalities. Characterising filament dynamics between and during reversals allowed us to inform a physical model of filament movement. This model captures observed reversal dynamics and predicts that the extent of cell-to-cell coupling in cellular decision of propulsion direction determines how coordinated reversals are. Based on this insight, we have found that longer filaments tend to loose coordination during reversals and that this de-coordination is linked with the formation of plectonemes. The presented findings quantify individual filament movement and provide a physical model of gliding motility that is consistent with experimental observations. This model will inform future studies on the molecular and physical mechanisms of force generation and collective behaviour of filaments.

4 Results

***F. draycotensis* filaments feature distinct fluorescent protein complexes on cell membranes, and are encased in slime.** Gliding motility in several single-celled bacterial species is found to be associated with rotation of the cell body around its long axis [14, 4]. Rotation is also mentioned in some gliding filamentous cyanobacteria [15, 18]. In none of these cases have rotation dynamics been quantified. Here, we explored rotation of *F. draycotensis* filaments using TIRF microscopy, which uses a narrow band of illumination ($\approx$ 200 nm) to focus solely on cellular membranes. The use of TIRF microscopy revealed that the cells of *F. draycotensis* contain fluorescent protein complexes on their membrane, localised predominantly near the poles of individual cells (Fig. 1A and Supplementary Movie S 1). These complexes display fluorescence when illuminated with a wavelength of 473 nm, but not 640 nm, consistent with their distinct tinge in colour micrographs (Fig. 1B and C). Similar surface features have been previously mentioned in other filamentous cyanobacteria species such as *Geitlerinema* and at times assumed to be cyanophycin granules. However, this is unlikely for the complexes described here, given their spectral properties.

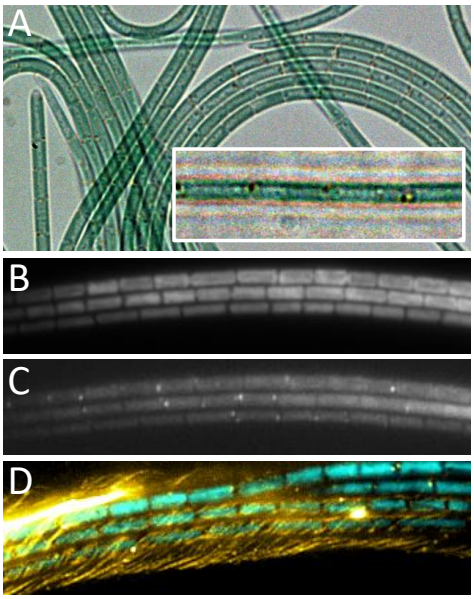

Figure 1: **(A)** Colour micrograph of *F. draycotensis* filaments. Inset: Presence of visible cell surface features, exhibiting a distinct colour. **(B)** TIRF image of filaments illuminated with light of wavelength 640nm. **(C)** Same filaments under 473nm light, showing regularly placed fluorescent protein complexes. **(D)** TIRF image of a bundle of filaments (colored cyan) surrounded by a sheath of exopolysaccharide (yellow), stained using Concanavalin-A.

Slime secretion accompanies gliding motility in all species studied to date. Several studies have also shown that deletion of genes involved in slime biosynthesis or secretion abolishes gliding motility [23]. However, studying the relation between slime and motility is difficult, as most dyes staining slime also stain common substrates used in microscopy, such as agar and glass slides. To better understand the location of slime in relation to cells, we performed TIRF on filaments that are stained with fluorescently labelled Concanavalin A (see *Methods*). This allowed the slime around the cell body to be distinguished from background staining of agar and showed that slime surrounds filaments as a tubular structure (Fig. 1D and Movie S 2). There are both empty and filament-containing slime tubes visible, and the fluorescent staining of these is enhanced in a helical pattern (Fig. 1D). Interestingly, the angle of this enhanced staining - of about 30 degrees - matches the observed angles of fibrillar arrays, that are described on the cell surface of several filamentous cyanobacteria species [15, 18].

Tracking of membrane protein complexes reveals rotation of filaments, tightly coupled to their translation. We utilised the fluorescence of the above-described membrane-bound protein complexes, to track their motion during filament gliding. We found that the movement of these protein complexes matches 2-dimensional projections of a 3-dimensional

helical trajectory (Fig 2A, see also Supplementary Figure S1 and Movie S 1). The angle θ, that the trajectories of the protein complexes form with the long axis of the filament, is very similar across different filaments. We collected 400 trajectories from 10 different filaments and found that the mean θ is 18 ± 2 degrees (Fig. 2B). Interestingly, all the observed helices had the same sign of the angle θ. This well-defined helix appears to be a constraint of motion, as we found that the linear velocity of gliding and angular speed are linearly well correlated, pointing towards motion with a low amount of slipping (Fig. 2C). This could indicate either a helical force generation or a screw-like structure on the cell exterior that translates linear into rotary motion.

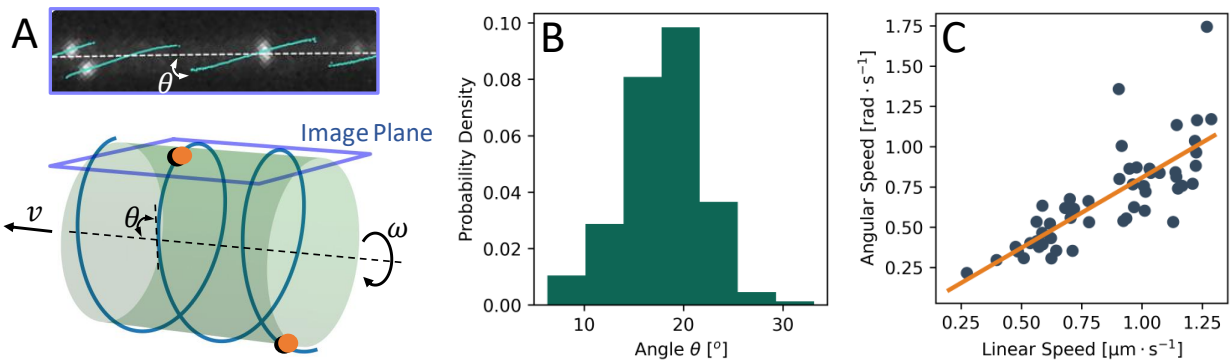

Figure 2: **(A)** Total Internal Reflection Fluorescence (TIRF) microscopy image. Excited using a $\lambda_{\text{ex}} =$ 473nm laser, with emission $\lambda_{\text{em}} > 550$nm. This image shows a thin (≈ 200 μm) section of the cell membrane. Over time, we measured the positions of the protein complexes as the filament glides and rotates, and calculated the angle θ between their trajectories and the long axis of the filament. Below the image, we display a helical trajectory, wrapping around a cylinder (representing the cell), reconstructed from experimental measurements. The blue rectangular frame signifies the plane from which the image in the top panel has been sampled. **(B)** Distribution of angles θ over a population of 10 filaments from different experiments. **(C)** The dependency of angular velocity ω, shown on the y-axis, on the linear gliding speed v, shown on the x-axis.

Filament movement on agar displays well-defined trajectories and a specific distribution of waiting times during reversals. We found that in low-magnification phase microscopy of filaments moving on agar, it is possible to distinguish a region of different phase contrast, which aligns perfectly with the trajectories of the filaments, and forming a 'track' (Fig. 3A and Movie S 3). Lone filaments' trajectories are mostly confined to these tracks, although they can sometimes derail from a given track and in most of these cases, join another track (Movie S 4). We conjecture that these tracks, visible in phase microscopy, are either the slime tubes themselves, or are deformations on the agar, caused by the slime secretion or filament movement, and that they confine the movement of the filaments on agar. In line with the latter hypothesis we found that filaments entering a circular track do not readily reverse direction (Movie S 5).

Regardless of their nature, the emergence of tracks during movement on agar allowed us to study movement dynamics within tracks and quantify reversal dynamics. We imaged filaments at low magnification, with images taken every 5 or 10 seconds, and quantified filament position and speed along a track. All analysed filaments displayed an oscillatory speed profile across their movement on the track (Fig. 3B). In other words, filament speed peaked at the midpoint of the track and filaments slowed down to a stop just before reversals. We then analysed the time filaments spent stopped (or nearly stopped) during a reversal, which we call

the "dwell time". Analysing over 400 reversal events for individual ends of a filament, leading or trailing, across 23 filaments, we found that dwell times displayed a long-tailed distribution (Fig. 3C). Most reversals happened within one or two frames, indicating dwell times shorter than 5 to 10 seconds, while a minority of reversals involved significant time spent stationary. We found that there was no clear difference between dwell time of leading and trailing ends of the filament (Fig. S2).

To better understand what happens during a reversal at the single cell level, we analysed reversal events with TIRF microscopy at high magnification and high frame rate (images taken every 33ms). Using $\lambda_{\text{ex}} = 473$nm laser to visualise the described protein complexes on each cell, we were able to track individual cells' motion during a reversal. We found that cells across the filament mostly stayed in synchrony during a reversal and displayed a steep acceleration immediately after a reversal (Fig. S1 and Movie S 1). In some filaments, however, we have seen individual cells displaying bursts of changes in speed and some cells initiating reversal earlier than others (Fig. S1 and Movie S 1). While we cannot rule out a role for fluorescence and imaging noise in these observations, they suggest the possibility of independent movement dynamics at single cell level during and before a reversal. Additionally, we note that the high acceleration of all cells after a reversal suggests torsional forces developing along the filament during a reversal event.

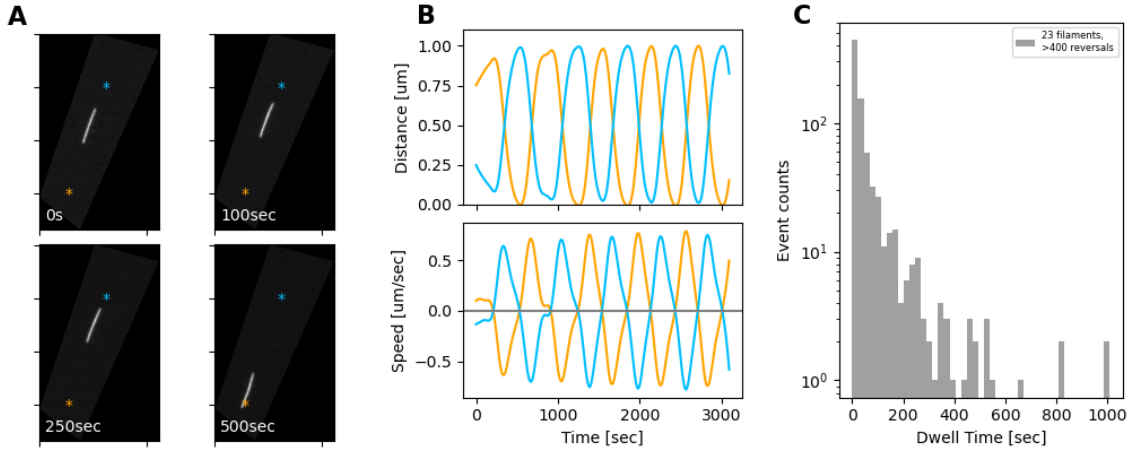

Figure 3: **(A)** A single filament shown at different points of movement (on agar). Time-lapse images were captured at 10 second intervals using fluorescence microscopy. The extreme points of the trajectory across the time lapse are marked in blue and orange points. **(B) Top:** Position of each end, calculated as distance to the respective extreme ends of the trajectory, shown with blue and orange asterisks on panel A. **Bottom:** Speed of each end, as calculated from the respective distance data. **(C)** Distribution of dwell times, as calculated from analysis of over 400 reversals from 23 filaments. For each filament, dwell time is taken as the time when speed was below 10 percent of the maximum.

A physical model captures filament movement dynamics and highlights a role for cell-to-cell coordination for smooth reversals. To better evaluate the observations on motility dynamics, we developed a minimalist 1-dimensional physical model that considers cells in a filament as coupled springs (see Fig. 4A and *Methods*). In this model, we implement mechano-sensing by each cell of any external and internal forces, which influences their "decision" to generate a propulsive force in either direction (see *Methods* and Eqs. (3),(6)). This decision acts in a way to change cellular propulsion direction in order to reduce any mechanical stress (compression/extension) on the cell. In other words, the model assumes that each cell can integrate forces from neighboring cells (as well as any external forces); based on these forces, the "decision" mechanism tunes the propulsion direction of the cell, so to reduce its own compression or extension. Additionally, we introduce a cellular memory that limits cells ability to switch force direction if they have recently done so (see Eqs. (3),(4) in *Methods*). Given this model, we simulated filaments confined to a track,

implemented as an external force field. For appropriate choice of parameters, we found that this model can produce self-sustained back-and-forth movement with reversals at the end of track bounds (Fig. 4A,B), in qualitative agreement with the smooth reversals reported in Fig. 3. Further, the distribution of dwell times, computed from simulations (Fig. S3), is also in qualitative agreement with experimental results.

We next run simulations to explore how the strength of cell-to-cell coupling for cellular decisions (i.e. the strength of mechano-sensing) affects reversal dynamics. In order to assess the performance of the filaments in performing coordinated reversals, we considered a fixed time window and counted the number of observed reversals during this period. We normalized this number over the estimated number of reversal of an ideal filament, that reverses smoothly and deterministically. We find that this ratio, which represents the extent of coordinated reversals, is sensitive to the strength of the mechano-sensing among cells and shows a non-monotonic behaviour, with an optimal value that depends on the filament length (see Fig. S4). This non-monotonic dependence between strength of mechano-sensing and extent of coordinated reversals appears to be fairly robust to changes in the cellular memory parameter, that controls how fast cells can respond to sensing (see Fig. S5). We observe, however, that larger values of the memory parameter requires stronger mechano-sensing to achieve smooth reversals (Fig. S5). The proposed model shows the importance of coordination among cells for establishment of smooth reversals. Indeed, when the mechano-sensing strength is reduced significantly, reversals become more erratic (see Fig. S6).

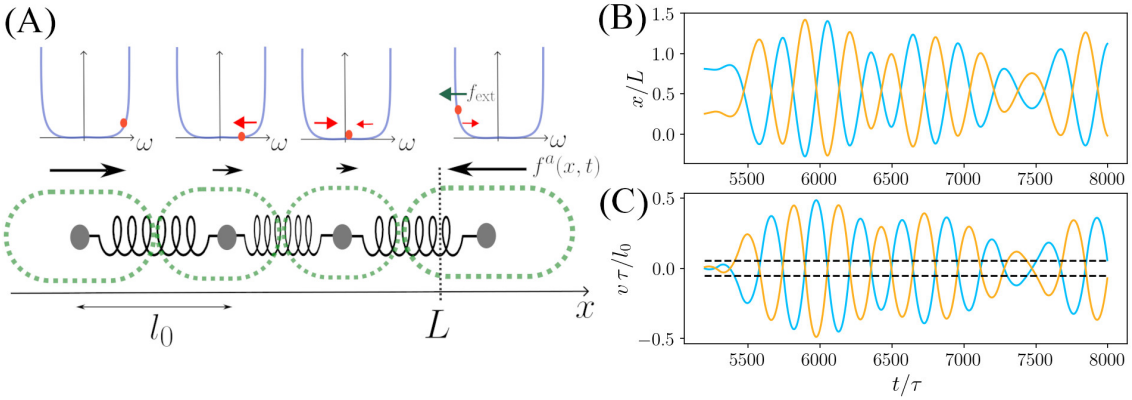

Figure 4: (A) A cartoon of the biophysical model (see Sec. 6). Cells are modelled as beads, connected by springs, with preferred rest length l_0. Cells self-propel with a propulsion force f_a. It is assumed that cells regulate the direction of f_a, and this regulation is modelled by a function ω, which includes a self-regulatory element, implemented as a confining potential U_ω (shown as blue lines in the panels above cells). The value ω_i of each cell is represented with an orange dot and its affected by random fluctuations, a mechanical feedback from neighbouring cells (V_ω, red arrows), and an external signal f_{ext}, present at the ends of the track L (green arrow) (see Eq. (5)). **(B)** An example simulation result, showing the trajectory of the filament and presented as in Fig. 3B. **(C)** Velocity of filament ends, computed from the simulated trajectory shown in panel (B), as a function of time. In (B) and (C), τ and l_0 are the simulations units of time and length, respectively. Simulated parameters are (in reduced units) N =30, L =60, ω_{max} =10, f_{ext} =5, K_ω =5. Dashed lines in (C) mark the interval below which the velocity of the leading/trailing cell is below 10% of its maximum.

Model predicted de-coordination during reversals is observed experimentally, together with plectoneme formation. To see whether the model-predicted break-down of cellular coordination can happen, we aimed at tracking longer filaments (see *Methods*). This analysis revealed several instances of filaments resulting in buckling in their middle sections, and sometimes in plectoneme formation, especially when moving on glass (see Supplementary Movie S 6- 9). A representative, example case from movement on agar is shown on Figure 5 (see also the associated Movie S 6). In this example, the movement starts in a similar way to most cases analysed on agar, with an oscillating speed profile and the two ends of the

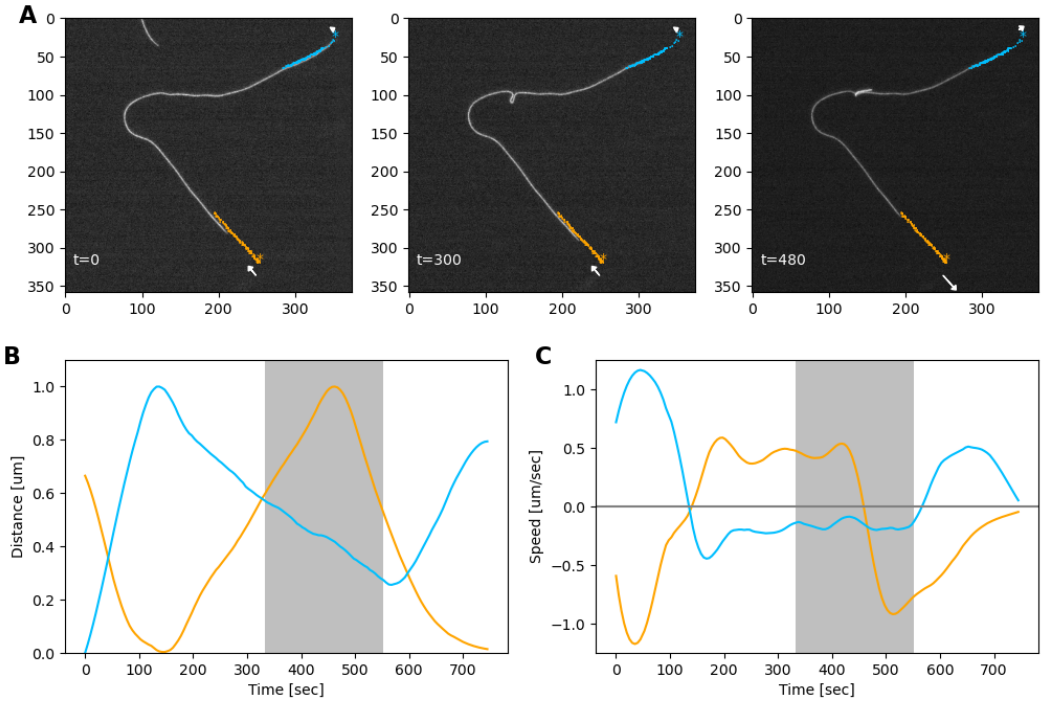

Figure 5: **(A)** A plectoneme forming filament shown at different points of movement (on agar), as shown on each image. Time-lapse images were captured at 10 second intervals using fluorescence microscopy. The orange and blue points indicate the tracked position of each end, while the same colored asterisk show the extremities of the movement. The arrows indicate speed of each end, with arrow length calculated from the difference in position between the time of the image and an image taken 20 frames later. **(B)** The position of the two ends of the filament over time. Ends are arbitrarily labelled as blue and orange, while position is calculated as distance to the respective extreme ends of the trajectory, shown on panel A. **(C)** Speed of each end, as calculated from the respective position data shown in panel B. The shaded area on the x-axis, on panels B and C, indicate the period in which the plectoneme is observed (see corresponding supplementary Movie S 6).

filament being coordinated in terms of position and speed (Fig. 5B). With the start of plectoneme formation, however, this coordination gets disrupted, with one end moving faster than the other, and finally reversing independently of the other end (Fig. 5B). This de-coordination seems to resolve towards the end of the recorded movement sequence, when the plectoneme resolves (Fig. 5 and Movie S 6).

Overall, we observed plectoneme formation relatively frequently, especially when filaments were moving on glass slides. Plectonemes sometimes resolved themselves and sometimes not, leading to formation of larger sections on a filament that can get "dragged" with the rest of the filament (Movie S 9). We note that these dynamics can be relevant for collective behaviors of multiple filaments, as plectonemes can sometime entangle other filaments and can lead to knot-like structures (Movie S 10).

5 Discussion and Conclusions

Here, we analysed the motion dynamics of the filamentous, gliding cyanobacterium *F. draycotensis*. We show that gliding on agar involves back-and-forth movement of filaments on well-defined trajectories. Filament speed oscillates throughout such movement, as filaments slow down towards the end of their trajectories and reverse. We find that the time spent in a reversal displays a long-tailed distribution, with most reversals taking shorter than 5 seconds, but some involving considerable time of filaments being stationary. Throughout their motion, including the reversal, cells in a filament remain highly coordinated. We show that these experimental observations can be recapitulated by a physical model that assumes individual force generation by each cell, mechanical-coupling among cells, and mechano-sensory (coordinated) control of force direction. This model suggests that the strength of such sensing-based coordination of propulsion direction is important for smooth reversals and reducing it can result in de-coordinated motion of filament ends. In line with this prediction, we find experimental evidence for filaments becoming occasionally de-coordinated, with their two ends moving independently and middle parts forming plectonemes. We hypothesize such dynamics to be linked with the loss of sensory coupling among cells, and de-coordination of the direction of their propulsive forces. We observed filaments to readily form plectonemes, especially when moving on glass, thereby resulting in de-coordinated motion of their two parts on either side of the plectoneme and entanglement. Taken together, these results provide a useful characterisation of gliding filaments' motion, which will inform future studies on both molecular mechanisms of force generation and collective behaviours of filaments.

In terms of molecular mechanisms, our finding that rotational and translational movement are closely coupled in *F. draycotensis* indicates a helical force generation. This coupling would be expected from a molecular model, such as those involving motor complexes moving on helical tracks around the cell [14, 4]. However, alternative models such as pili being pushed across helical fibrils could also explain this. Both fibrils and pili were observed in several gliding cyanobacteria, [15, 16, 17, 18], but how they could be interacting and how they might lead to rotation is not clear. We note that filament rotation is reported in the literature, alongside presence of fibrillar arrays, but without any quantification of the former [15, 18]. We also note that our observation of enhanced helical staining of the slime displays an angle closely matching that of observed fibrillar arrays [15, 18]. Recent studies from *Nostoc* species indicate propulsion to result from pili extension [5, 20], but whether and how this relates to rotation in that species, which does not seem to have fibrillar arrays [18], is unclear. Future application of TIRF microscopy in different species can further clarify the translation-rotation coupling in filamentous cyanobacteria and can help to reveal rotating and non-rotating gliding modalities.

Phototaxis is implied in several gliding filamentous cyanobacteria [23, 27, 28], but a fully quantitative analysis of photoresponses at the single filament level is currently lacking. In this context, an interesting observation we made in this study is the presence of fluorescent, membrane-bound protein complexes. We hypothesize that these complexes are associated with light sensing, since our tracking of them in TIRF microscopy always coincided with reversal of filaments. Thus, it is possible that the wavelength at which they get excited (437nm laser used in TIRF microscopy) is also acting as a sensory signal for reversals. This

possibility will be explored in a future study, along with further characterization of any phototaxis behavior in *F. draycotensis*.

Gliding motility in filamentous cyanobacteria is commonly associated with aggregate or macro-scale structure formation. These formations are relevant in the context of physiological functions of the cyanobacteria, and their associated microbial communities, as shown in the case of *F. draycotensis* [26]. Similarly, in the case of the ocean-dwelling species of the *Trichodesmium* genus, aggregate formation is linked with the biogeochemically relevant processes of iron acquisition [29]. The results presented here show that de-coordination of cellular forces within a filament can lead to formation of plectonemes and knots, which can entangle multiple filaments together. Further studies of this process can elucidate how aggregate and macro-scale formations develop and inform their physical modelling.

Given that gliding motility is observed in phylogenetically diverse bacteria, it is possible for it to be underpinned by different molecular mechanisms and present different motion dynamics. The inter-connectivity of propulsion and slime secretion is difficult to disentangle purely by molecular approaches, and development of physical models solely based on identified proteins can be limited. In particular, drastically different physical models can be constructed from observed molecular constituents. We advocate coupling of molecular studies with detailed analysis of motion dynamics, as quantification of these can provide an additional framework to constrain and test different models, ultimately providing a more complete understanding of gliding motility and associated collective behaviors.

6 Methods

Sampling and Culturing Cultures of *F. draycotensis* were grown in medicinal flasks, in volumes of 30 mL BG11+ with added vitamin mix as described previously [26]. Cultures were kept under visible light irradiance of $\approx 30\ \mu\mathrm{M} \cdot \mathrm{photons} \cdot \mathrm{m}^{-2}\mathrm{s}^{-1}$, across a repeating 12-hour light/12-hour dark cycle. Samples were obtained from cultures aged between 4 and 8 weeks, by withdrawing 0.5 mL of material containing several pieces of biofilm, transferring the aliquot into a 1.5 mL microfuge tube and vortexing for 1 minute to break up the material. If the mixture was not homogeneous, additional mixing was performed using a 1 mL mechanical pipette.

Sample Preparation for Imaging Prior to imaging, collected innoculate was diluted into fresh BG11+ media with vitamin mix to a desired dilution (typically 1:50). For microscopy performed with $1.5 - 2\%$ agarose pads [30], 3μL of the homogenised diluted sample was added to the pad. The droplet was then left to dry for 10-15 minutes, depending on the age of the agarose pad and room humidity. Where stated, the agarose pad was flipped onto a 22×50 mm cover glass, sandwiching the sample between the agarose and the glass. Otherwise, the sample was left on top of the agarose and the pad placed in a cover glass bottomed dish (MatTek/CellVis) for microscopy.

As described, some samples were imaged inside a millifluidic chamber device (Ibidi μ-Slide III 3D Perfusion) or on glass slides, using a 1.5 × 1 cm Gene frame (Thermo Scientific) as a spacer. For glass slide samples, the Gene frame sticker was placed on the standard glass slide. To the frame 200 μL of diluted sample was added, and the chamber was sealed with a cover glass.

Regardless of sample preparation method, all prepared samples were left to settle for 30-60 minutes, being kept on a laboratory bench under room temperature and illumination.

Imaging Conditions Light microscopy was performed on an Olympus IX83 microscope, using a CoolLED pE-300 illumination system. Imaging was performed using a Cool-HQ2, with a typical imaging rate of 5-10 seconds. The stage is enclosed in an environmental chamber and stabilised at 25°C. Phase imaging was performed with a low exposure rate (≈ 5 ms). Chlorophyll fluorescence was measured through a Chroma DSRed filter cube, with a recorded excitation light power of 17.4 mW and an exposure time of 100 ms. TIRF imaging was performed on a standard NanoImager system (ONI).

Image Analysis Images were analysed with custom-written software in Python. Analyses involved tracking individual filaments or membrane complexes on each cell, across time-lapse images. In the case of filament tracking, movies of a larger field of view were cropped to focus on single filaments, and these were processed by fitting a contour on the filament and deriving a mid-point spline from this. By repeating this process across each image in a time-lapse, it was possible to track the position of trailing and leading ends of the filament and their speed. In the case of longer time-lapse movies, any drift in the images was stabilised using stationary filaments within the larger field of view. All code used in these analyses are made available on a Github repository; https://github.com/OSS-Lab

Biophysical model We model cyanobacteria as out-of-equilibrium filaments in 1 dimension. The filament is composed by N beads that represent cells in a cyanobacteria filament. The position of bead i is denoted by x_i ($i = 1..N$). Beads are connected with their nearest neighbours, along the filament, by harmonic springs. Each bead follows an over-damped equation of motion, given by;

$$\dot{x}_i = \frac{1}{\gamma}\left(-\frac{dV}{dx_i} + f_i^a \cdot s_i(x,t)\right) + \xi_i(t) \tag{1}$$

where γ is the friction coefficient and $\xi_i(t)$ is a Gaussian white noise, following $\langle \xi_i(t)\xi_j(t')\rangle = 2k_BT/\gamma\delta_{ij}\delta(t-t')$, T being the temperature. The potential energy $V(x)$ reads

$$\beta V(x) = \sum_{i=1}^{N-1} \frac{1}{2}\beta K((x_{i+1} - x_i) - l_0)^2 \tag{2}$$

where $\beta = 1/k_BT$ is the inverse of the thermal energy (k_B is the Boltzmann constant) and K is the spring constant, representing the elastic response of the cell upon compression or extension. The rest length l_0 =1 represents the unperturbed (average) length of a cell. The remaining term in Eq. (1) represent the beads' self-propulsion, i.e. there is a force $f_i^a(x,t) = f_i^a \cdot s_i(x,t)$, generated by the bead itself, that causes it to move in the positive or negative direction. The f_i^a is defined as a constant in time, while $s_i(x,t)$ sets the "active state" of bead i at position x and time t. We set $s_i(x,t)$ to be a continuous variable, such that $-1 < s_i(x,t) < 1$. Thus, a cell can be propelled in the positive ($s_i(x,t) \approx +1$) or negative ($s_i(x,t) \approx -1$) x direction or it can be inert ($s_i(x,t) \approx 0$).

To model the process of reversals, we envision that each cell can decide on the direction of its propulsive force. This idea is motivated by the fact that all studied uni-cellular gliding bacteria incorporate directional change, and individual cells in filamentous cyanobacteria are observed to change the location of their Type IV pili apparatus across the cell poles [20, 5]. To model cellular direction change, we introduce a function, $\omega_i(x,t)$, describing the internal "state" of each cell and dictating its active state by the relation $s_i(x,t) = \tanh(\omega_i(x,t))$. From a biological perspective, $\omega_i(x,t)$ abstract the behavior of a cellular signalling network that integrates external and internal inputs for the cell and sets its propulsive direction. To this end, we define $\omega_i(x,t)$ as integrating several inputs, as follows:

$$\dot{\omega}_i(x,t) = \frac{1}{\gamma_\omega}\left(-\frac{dU_c}{d\omega_i} - \frac{dV_\omega}{dx_i} + f_{\text{ext}}(x,t)\right) + \eta_i(t) \tag{3}$$

where γ_ω is a friction coefficient, $\eta_i(t)$ is a Gaussian white noise, U_c is a confinement potential, $f_{\text{ext}}(x,t)$ is an (adimensional) external force field, and V_ω is a mechano-sensing (adimensional) potential. The confinement potential is a mathematical abstraction that allows us to maintain the output of $\omega_i(x,t)$ in a finite interval. This potential is given by:

$$U_c(\omega) = \begin{cases} \frac{1}{2}A(|\omega| - \omega_{\max})^4 & |\omega| > \omega_{\max} \\ 0 & \text{otherwise} \end{cases} \tag{4}$$

with $A = 1$. The parameter $\omega_{\max}$ determines the extreme values that $\omega_i(x,t)$ can attain. As such, this parameter acts as a memory term; when given terms in Eq. (3) push it in one direction, $\omega_{\max}$ will determine

the time when their effects will start changing $\omega_i(x,t)$.
The noise term captures any fluctuations, either internal to the cellular signalling networks or caused by external noise (thermal or otherwise). It ensures that the individual cells can also turn on or off or switch direction spontaneously. The noise term $\eta_i(t)$ follows $\langle \eta_i(t)\eta_j(t')\rangle = 2D_\omega \delta_{ij}\delta(t-t')$, with $D_\omega = k_B T_\omega/\gamma_\omega$ a diffusion coefficient, and T_ω being the temperature that characterises the magnitude of the fluctuations of ω in absence of external stimuli.
Following the experimental observations, we postulate the existence of a specific external stimulus that keeps filaments on a well-defined trajectory on agar, i.e. a track. We assume for simplicity that the track is fixed and extends from $x/l_0 = 0$ to $x/l_0 = L$. The external stimulus field is given by the following functional form:

$$f_{\text{ext}}(x,t) = \begin{cases} f_{\text{ext}} & \text{if } x < 0 \\ -f_{\text{ext}} & \text{if } x > L \\ 0 & \text{else} \end{cases} \tag{5}$$

where f_{ext} is an adimensional constant. Given Eq. (3), the action of the external field drives the auxiliary variable to positive/negative values.
The potential V_ω encodes the mechano-sensitivity of each cell to their neighbors and is given as;

$$V_\omega(x) = \sum_{i=1}^{N-1} \frac{1}{2} K_\omega((x_{i+1} - x_i) - l_0)^2 \tag{6}$$

where the quantity $K_\omega = f_{\text{ext}}/l_0 + \delta K_\omega$ is an effective spring constant. The function V_ω encodes the feedback to a mechanical stress (compression/extension) applied on the cell, compelling the direction of the self-propulsion so that this stress is relieved.
Notice that, within the model, f_{ext} essentially encodes the basal strength of the response of the cells to stimuli, either extra- or inter-cellular. The mechano-sensing can be more ($\delta K_\omega > 0$) or less ($\delta K_\omega < 0$) relevant than the external stimulus; naturally, we impose $\delta K_\omega > -|f_{\text{ext}}|$, i.e. there can not be a positive feedback to compression.

Simulation details We integrate the equations of motion Eq. (1) using a stochastic predictor-corrector algorithm, while the equations Eq. (3) are integrated using the Euler-Maruyama algorithm. In both cases, we employ an integration time step $\Delta t = 10^{-3}\tau$, τ being the unit of time. As mentioned above, we set the average length of an unperturbed cell as the unit of length and set the unit of time as the diffusion time of a single inactive cell $\tau = l_0^2/2D_0$. For convenience, we set the unit of energy as the active "work" $\epsilon = f^a l_0 = 1$; as such, we fix f^a =1 throughout the simulations. We further fix the friction coefficient to $\gamma = 1\tau^{-1}$. We assume that the motion of the filament is dominated by its self-propulsion, i.e. $f^a l_0 \gg k_b T$ and we set $k_B T = 0.01\epsilon$.
Concerning the parameters that enters in the evolution of ω, the scale of the "energy" should be set here by $k_B T_\omega$. However, we set $k_B T_\omega = 0.1$ for convenience; we find that reasonably smooth reversals can be obtained for such a choice, maintaining the other parameters within the same order of magnitude. Indeed, we fix $f_{\text{ext}} = 5$.
The analysis of the simulation results focuses on the dwell time and the number of reversals. The dwell time is computed as in the experiments: the simulated trajectory is smoothed via a spline and the velocity is computed from there. A dwell time is defined as the interval within which the velocity remains, in absolute value, below 10% of its maximal value. The number of reversals depends on the length of the trajectory, thus we normalise it by the quantity $n_r^{(e)} = \tau_{\text{sim}}/\tau_r^{(e)}$, with $\tau_r^{(e)} \approx (L - N\, l_0)/v$ and τ_{sim} the simulation time. The quantity $n_r^{(e)}$ is the number of reversals one would expect from an ideal filament, that reverses smoothly and deterministically in a negligible time and then travels at constant speed $v = f^a/\gamma$. As such the ideal time between two reversals is given by $\tau_r^{(e)}$, i.e. the time the trailing/leading cell would take to travel from its initial condition (after a reversal) to the track boundary.

7 Funding

This project is funded by the Gordon and Betty Moore Foundation (grant https://doi.org/10.37807/GBMF9200). E. L. acknowledges support from the MIUR grant Rita Levi Montalcini. M. P. acknowledges that IMEDEA is an accredited "María de Maeztu Excellence Unit" (Grant CEX2021-001198, funded by MCIN/AEI/10.13039/501100011033) María de Maeztu Excellence Unit (CEX2021-001198/AEI/10.13039/501100011033).

8 Acknowledgements

We acknowledge the help of imaging facility manager Ian Hands-Portman with microscopy setups and Dr. Nicole Robb for allowing access to her groups' TIRF microscopy.

9 References

[1] E. Hoiczyk. "Gliding motility in cyanobacterial: observations and possible explanations". In: *Arch Microbiol* 174.1-2 (2000), pp. 11–7. ISSN: 0302-8933 (Print) 0302-8933 (Linking). DOI: 10.1007/s002030000187.

[2] M. J. McBride. "Bacterial gliding motility: multiple mechanisms for cell movement over surfaces". In: *Annu Rev Microbiol* 55 (2001), pp. 49–75. ISSN: 0066-4227 (Print) 0066-4227 (Linking). DOI: 10.1146/annurev.micro.55.1.49.

[3] E. M. Mauriello et al. "Gliding motility revisited: how do the myxobacteria move without flagella?" In: *Microbiol Mol Biol Rev* 74.2 (2010), pp. 229–49. ISSN: 1098-5557 (Electronic) 1092-2172 (Linking). DOI: 10.1128/MMBR.00043-09.

[4] B. Nan. "Bacterial Gliding Motility: Rolling Out a Consensus Model". In: *Curr Biol* 27.4 (2017), R154–R156. ISSN: 1879-0445 (Electronic) 0960-9822 (Linking). DOI: 10.1016/j.cub.2016.12.035.

[5] A. Wilde and C. W. Mullineaux. "Motility in cyanobacteria: polysaccharide tracks and Type IV pilus motors". In: *Mol Microbiol* 98.6 (2015), pp. 998–1001. ISSN: 1365-2958. DOI: 10.1111/mmi.13242.

[6] J. Henrichsen. "Bacterial surface translocation: a survey and a classification". In: *Bacteriol Rev* 36.4 (1972), pp. 478–503. ISSN: 0005-3678 (Print) 0005-3678 (Linking). DOI: 10.1128/br.36.4.478-503.1972.

[7] R. N. Shepard and D. Y. Sumner. "Undirected motility of filamentous cyanobacteria produces reticulate mats". In: *Geobiology* 8.3 (2010), pp. 179–90. ISSN: 1472-4669 (Electronic) 1472-4669 (Linking). DOI: 10.1111/j.1472-4669.2010.00235.x.

[8] N. Sato et al. "Cellular Dynamics Drives the Emergence of Supracellular Structure in the Cyanobacterium, Phormidium sp. KS". In: *Life (Basel)* 4.4 (2014), pp. 819–36. ISSN: 2075-1729 (Print) 2075-1729 (Linking). DOI: 10.3390/life4040819.

[9] D. Kaiser. "Coupling cell movement to multicellular development in myxobacteria". In: *Nat Rev Microbiol* 1.1 (2003), pp. 45–54. ISSN: 1740-1526 (Print) 1740-1526 (Linking). DOI: 10.1038/nrmicro733.

[10] M. Sun et al. "Motor-driven intracellular transport powers bacterial gliding motility". In: *Proc Natl Acad Sci U S A* 108.18 (2011), pp. 7559–64. ISSN: 1091-6490 (Electronic) 0027-8424 (Linking). DOI: 10.1073/pnas.1101101108.

[11] B. Nan et al. "Myxobacteria gliding motility requires cytoskeleton rotation powered by proton motive force". In: *Proc Natl Acad Sci U S A* 108.6 (2011), pp. 2498–503. ISSN: 1091-6490 (Electronic) 0027-8424 (Linking). DOI: 10.1073/pnas.1018556108.

[12] D. Nakane et al. "Helical flow of surface protein required for bacterial gliding motility". In: *Proc Natl Acad Sci U S A* 110.27 (2013), pp. 11145–50. ISSN: 1091-6490 (Electronic) 0027-8424 (Linking). DOI: 10.1073/pnas.1219753110.

[13] B. Nan et al. "Flagella stator homologs function as motors for myxobacterial gliding motility by moving in helical trajectories". In: *Proc Natl Acad Sci U S A* 110.16 (2013), E1508–13. ISSN: 1091-6490 (Electronic) 0027-8424 (Linking). DOI: 10.1073/pnas.1219982110.

[14] L. M. Faure et al. "The mechanism of force transmission at bacterial focal adhesion complexes". In: *Nature* 539.7630 (2016), pp. 530–535. ISSN: 1476-4687 (Electronic) 0028-0836 (Linking). DOI: 10.1038/nature20121.

[15] L. N. Halfen and R. W. Castenholz. "Gliding in a blue-green alga: a possible mechanism". In: *Nature* 225.5238 (1970), pp. 1163–5. ISSN: 0028-0836 (Print) 0028-0836 (Linking). DOI: 10.1038/2251163a0.

[16] E. Hoiczyk and W. Baumeister. "Envelope Structure of Four Gliding Filamentous Cyanobacteria". In: *Journal of Bacteriology* 177.9 (1995).

[17] D.G. Adams, D. Ashworth, and B. Nelmes. "Fibrillar Array in the Cell Wall of a Gliding Filamentous Cyanobacterium". In: *Journal of Bacteriology* 181.3 (1999).

[18] N. Read, S. Connell, and D. G. Adams. "Nanoscale visualization of a fibrillar array in the cell wall of filamentous cyanobacteria and its implications for gliding motility". In: *J Bacteriol* 189.20 (2007), pp. 7361–6. ISSN: 0021-9193 (Print) 1098-5530 (Electronic) 0021-9193 (Linking). DOI: 10.1128/JB.00706-07.

[19] E. Hoiczyk. "Structural and biochemical analysis of the sheath of Phormidium uncinatum". In: *J Bacteriol* 180.15 (1998), pp. 3923–32. ISSN: 0021-9193 (Print) 0021-9193 (Linking). DOI: 10.1128/JB.180.15.3923-3932.1998.

[20] B. Khayatan, J. C. Meeks, and D. D. Risser. "Evidence that a modified type IV pilus-like system powers gliding motility and polysaccharide secretion in filamentous cyanobacteria". In: *Mol Microbiol* 98.6 (2015), pp. 1021–36. ISSN: 1365-2958 (Electronic) 0950-382X (Linking). DOI: 10.1111/mmi.13205.

[21] David M Zuckerman, Jeffery Man To So, and Egbert Hoiczyk. "Type two secretion systems secretins are necessary for exopolymeric slime secretion in cyanobacteria and myxobacteria". In: *bioRxiv* (2022), pp. 2022–03. DOI: 10.1101/2022.03.08.483542.

[22] Y. W. Cho et al. "Dynamic localization of HmpF regulates type IV pilus activity and directional motility in the filamentous cyanobacterium Nostoc punctiforme". In: *Mol Microbiol* 106.2 (2017), pp. 252–265. ISSN: 1365-2958 (Electronic) 0950-382X (Linking). DOI: 10.1111/mmi.13761.

[23] T. Lamparter et al. "The involvement of type IV pili and the phytochrome CphA in gliding motility, lateral motility and photophobotaxis of the cyanobacterium Phormidium lacuna". In: *PLoS One* 17.1 (2022), e0249509. ISSN: 1932-6203 (Electronic) 1932-6203 (Linking). DOI: 10.1371/journal.pone.0249509.

[24] U. Pfreundt et al. "Controlled motility in the cyanobacterium Trichodesmium regulates aggregate architecture". In: *Science* 380.6647 (2023), pp. 830–835. ISSN: 1095-9203 (Electronic) 0036-8075 (Linking). DOI: 10.1126/science.adf2753.

[25] M. K. Faluweki et al. "Active Spaghetti: Collective Organization in Cyanobacteria". In: *Phys Rev Lett* 131.15 (2023), p. 158303. ISSN: 1079-7114 (Electronic) 0031-9007 (Linking). DOI: 10.1103/PhysRevLett.131.158303.

[26] Sarah JN Duxbury et al. "Reproducible spatial structure formation and stable community composition in the cyanosphere predicts metabolic interactions". In: *bioRxiv* (2022), pp. 2022–12. DOI: 10.1101/2022.12.13.520286.

[27] E. L. Campbell et al. "Genetic analysis reveals the identity of the photoreceptor for phototaxis in hormogonium filaments of Nostoc punctiforme". In: *J Bacteriol* 197.4 (2015), pp. 782–91. ISSN: 1098-5530 (Electronic) 0021-9193 (Linking). DOI: 10.1128/JB.02374-14.

[28] W. Nultsch and D. P. Hader. "Photomovement in motile microorganisms–II". In: *Photochem Photobiol* 47.6 (1988), pp. 837–69. ISSN: 0031-8655 (Print) 0031-8655 (Linking). DOI: 10.1111/j.1751-1097.1988.tb01668.x.

[29] Nivi Kessler et al. "Selective collection of iron-rich dust particles by natural Trichodesmium colonies". In: *The ISME journal* 14.1 (2020), pp. 91–103. ISSN: 1751-7370. DOI: 10.1038/s41396-019-0505-x.

[30] Jerko Rosko et al. "Preparation of agarose pads suitable for viewing filamentous cyanobacterial microbial communities using time-lapse imaging". In: (2022). DOI: 10.17504/protocols.io.81wgb65p1lpk/v1.

10 Supplementary Information

10.1 Supplementary videos:

1. **Movie S1**- TIRF imaging of filaments in slime with a time interval of 33 ms. Slime stained with Concavalin A and false-colored in yellow. Cyano filaments' auto fluorescence is false colored in cyan. AVI produced with 60 fps compression. Link: https://youtu.be/hYTLHQCJSUU

2. **Movie S2**- TIRF imaging of filament undergoing a reversal, where the fluorescence shows the protein complexes on the surface. Time interval of 33 ms. AVI produced with 100 fps compression. Link: https://youtube.com/shorts/1ZvlS8daQko

3. **Movie S3**- Single filament in track. Magnification x10 (0.645 um/pixel), and a time interval of 5 seconds. Filaments placed on top of 2.5 % BG11+ agar. Phase image with 5 ms exposure. AVI produced with 20 fps compression. Link: https://youtube.com/shorts/hYRJ7QpGD-g

4. **Movie S4**- Several filaments in tracks. Magnification x10 (0.645 um/pixel), and a time interval of 5 seconds. Filaments placed on top of 2.5 % agarose with BG11+. Phase image with 5 ms exposure. AVI produced with 20 fps compression. Link: https://youtu.be/U4kxmlG9gWw

5. **Movie S5**- Single filament on a circular trajectory. Magnification x4 (1.61 um/pixel), and a time interval of 5 seconds. Filaments placed under 1.5 % agarose with BG11+. Fluorescence recorded in Red channel with 100 ms exposure. AVI produced with 20 fps compression. https://youtu.be/hDORLFTr7hQ

6. **Movie S6**- Buckling filament. Magnification x4 (1.61 um/pixel), and a time interval of 5 seconds. Filaments placed under 1.5 % agarose with BG11+. Fluorescence recorded in Red channel with 100 ms exposure. AVI produced with 20 fps compression. Link: https://youtu.be/7jkSTfb08lM

7. **Movie S7**- Filament with a plectoneme formation in the middle. Magnification x10, time interval of 30 seconds. Filaments placed inside Ibidi chamber. AVI produced with 20 fps compression. Link: https://youtu.be/7SZLcaZ8MFY

8. **Movie S8** - Plectoneme formation. Magnification x10. Filaments placed inside Ibidi chamber. AVI produced with 20 fps compression. Link: https://youtu.be/BFRHtVQPoUA

9. **Movie S9**- Plectoneme formation. Magnification x10. Filaments placed inside Ibidi chamber. AVI produced with 20 fps compression. Link: https://youtu.be/vK4BWFr_k2o

10. **Movie S10**- Plectoneme formation with samples placed on glass slide with chamber. Magnification x4 (1.61 um/pixel), and a time interval of 10 seconds. Fluorescence recorded in Red channel with 100 ms exposure, phase image with 5 ms exposure. AVI produced with 20 fps compression. Link: https://youtu.be/snEczQBk0dk

10.2 Supplementary figures:

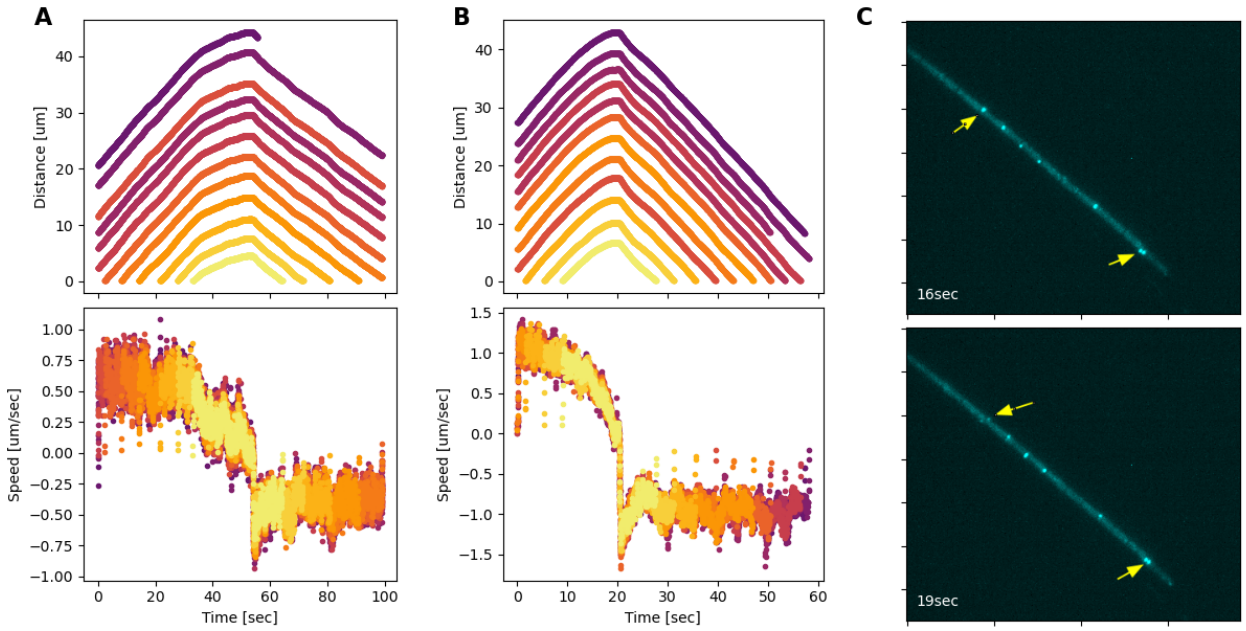

Fig. S1: (A and B, top row). Time evolution of the position of membrane-bound protein complexes compared to their initial position at the beginning of the timelapse. Each line shows the data for a an individual complex located on one cell. Note that some cells move out of the field of view earlier than others. **(A and B, bottom row)**. Speed of membrane-bound protein complexes, calculated from position data shown on the top rows. A and B show results from two representative filaments, with others displaying similar dynamics. **(C)** Two time points in the movement sequence of a filament, the position and speed data for which is shown in panel B. The location of two protein complexes are shown with arrows, indicating that the complex further up the filament starts its movement earlier than the one at the tip of the filament. See also the associated Supplementary Movie S2.

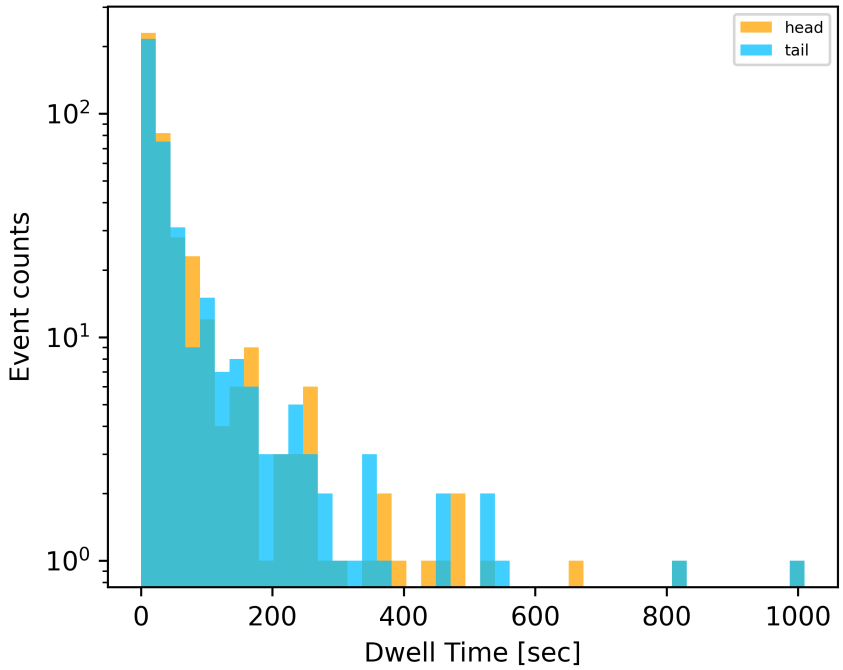

Fig. S2: Distribution of dwell times of leading (head) and trailing (tail) ends of filaments. Data is collated from 23 filaments, undergoing over 400 reversals for each end.

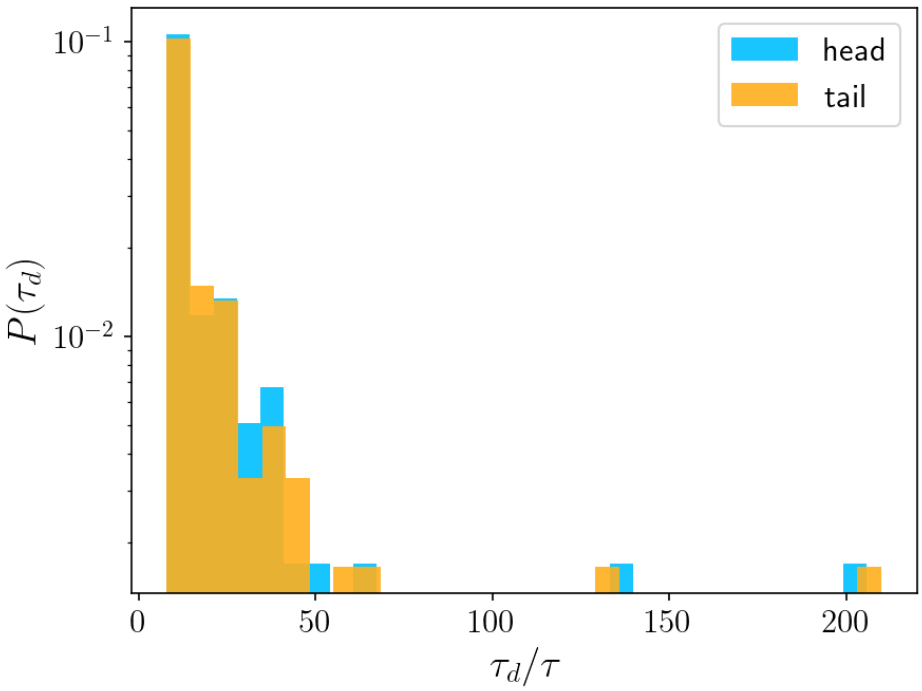

Fig. S3: Simulated distribution of dwell times of leading (head, orange bars) and trailing (tail, blue bars) ends of the filament. The parameters values are as in Fig. 4.

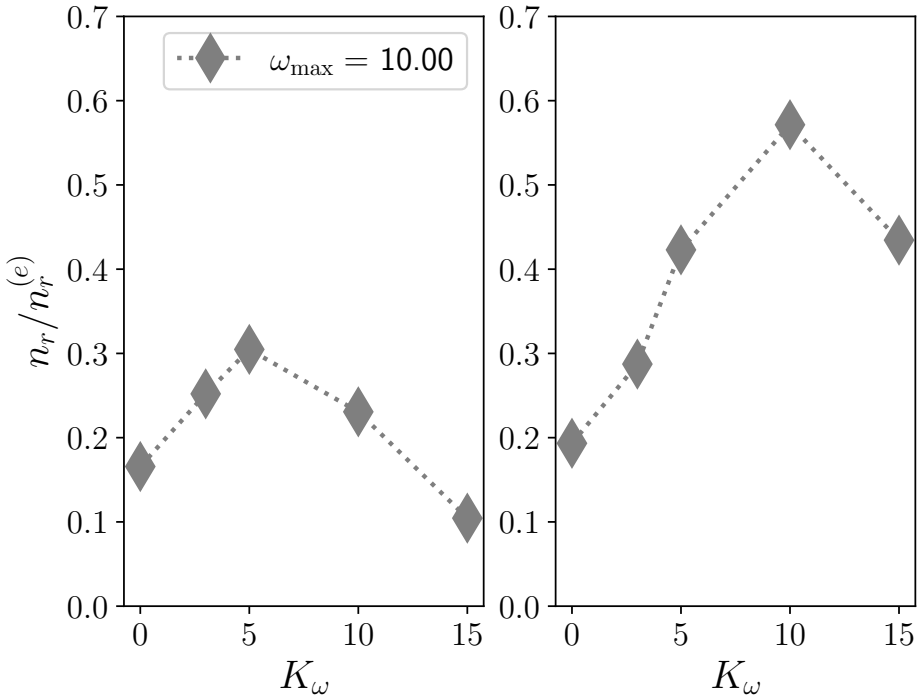

Fig. S4: Number of reversals n_r over the number of expected reversals $n_r^{(e)}$ as a function of the mechano-sensing coupling K_ω. Parameters used are, (A) N =30, L=60 (B) N =50, L=100. Other parameters as in Fig. 4. The definition of n_r and $n_r^{(e)}$ is reported in Sec. 6 (Simulation details).

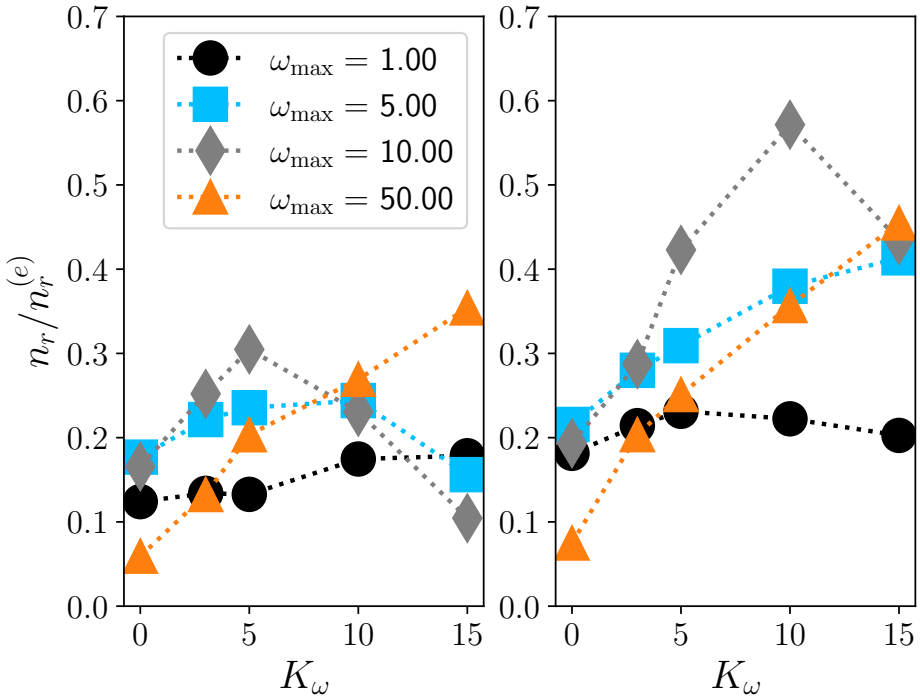

Fig. S5: Number of reversals n_r over the number of expected reversals $n_r^{(e)}$ as a function of the mechano-sensing coupling K_ω for different values of $\omega_{\max}$; (A) N =30, L=60 (B) N =50, L=100. Other parameters as in Fig. 4. The definition of n_r and $n_r^{(e)}$ is reported in Sec. 6 (Simulation details).

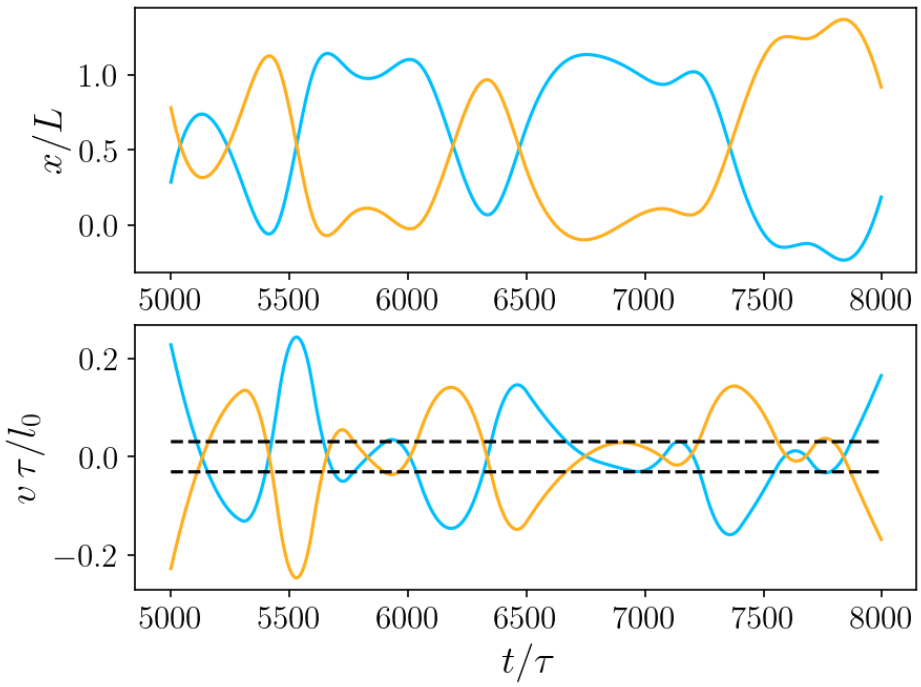

Fig. S6: (A) An example simulation result, showing the temporal trajectory of each end of the filaments, in the case cells have no mechano-sensing of the neighbouring cells. Trajectories are represented as in Fig. 3B. (B) Velocity of filament ends, computed from the simulated trajectory, as a function of time (reported as in Fig. 3C). In both panels, τ and l_0 are the simulations units of time and length, respectively. Simulated parameters are (in reduced units) N =30, L =60, ω_{max} =10, f_{ext} =5,, K_ω =0. Dashed lines in (C) mark the interval below which the velocity of the leading/trailing cell is below 10% of its maximum.